SOFT ROBOTICS
Volume 00, Number 00, 2017

DOI: 10.1089/soro.2017.0018

SoRo
Soft Robotics

ORIGINAL ARTICLE

Compliant Buckled Foam Actuators and Application in Patient-Specific Direct Cardiac Compression

Benjamin C. Mac Murray,[1] Chaim C. Futran,[2] Jeanne Lee,[2] Kevin W. O'Brien,[2] Amir A. Amiri Moghadam,[3,4] Bobak Mosadegh,[3,4] Meredith N. Silberstein,[2] James K. Min,[3,4] and Robert F. Shepherd[2]

Abstract

We introduce the use of buckled foam for soft pneumatic actuators. A moderate amount of residual compressive strain within elastomer foam increases the applied force $\sim 1.4\times$ or stroke $\sim 2\times$ compared with actuators without residual strain. The origin of these improved characteristics is explained analytically. These actuators are applied in a direct cardiac compression (DCC) device design, a type of implanted mechanical circulatory support that avoids direct blood contact, mitigating risks of clot formation and stroke. This article describes a first step toward a pneumatically powered, patient-specific DCC design by employing elastomer foam as the mechanism for cardiac compression. To form the device, a mold of a patient's heart was obtained by 3D printing a digitized X-ray computed tomography or magnetic resonance imaging scan into a solid model. From this model, a soft, robotic foam DCC device was molded. The DCC device is compliant and uses compressed air to inflate foam chambers that in turn apply compression to the exterior of a heart. The device is demonstrated on a porcine heart and is capable of assisting heart pumping at physiologically relevant durations (~ 200 ms for systole and ~ 400 ms for diastole) and stroke volumes (~ 70 mL). Although further development is necessary to produce a fully implantable device, the material and processing insights presented here are essential to the implementation of a foam-based, patient-specific DCC design.

Keywords: direct cardiac compression, elastomer foam, pneumatic actuation, patient-specific device

Introduction

Compliant actuators, relative to their rigid counterparts, uniquely have an increased potential for safe human–robot interaction due to their infinite passive degrees of freedom actuated at low mechanical stresses, a high number of possible degrees of freedom of motion, and an ability to adapt their shape to changing environments.[1] This class of actuators includes piezoelectric polymers,[2] electroactive polymers,[3] dielectric elastomer actuators,[4] thermo- and chemically responsive gels,[5] and fluidically pressurized elastomer actuators.[6] Of these, fluidically pressurized elastomer actuators are a good choice for applying high forces and actuating at high speeds[7] within low-density and highly stretchable systems. To transport fluid for actuation, fluidically pressurized elastomer actuators require fluidic channels and chambers,[8,9] the design and fabrication of which limit their geometry, often necessitating complex molding and/or assembly to form fully 3D machines.

Foam actuators simplify this fabrication process by eliminating the need for designed channels and chambers. The elastomer foam itself serves as the inflation chamber, while the interconnected porous network serves as fluidic channels. When sealed within a nonporous elastomer, these foams form a fluidic actuator enabling 3D soft machines without complex assembly[10,11] or investment casting.[9,12] While these actuators can function using air, water, and other fluids as the pressurizing medium, we used compressed air as the actuating fluid for all actuators due to the inviscid nature of air and fast transport through micropores.[13] These foam actuators, however, experience reduced actuation amplitudes. Because they comprise ≥60% void space, less material participates in

Departments of [1]Materials Science and Engineering and [2]Mechanical and Aerospace Engineering, Cornell University, Ithaca, New York.
[3]Department of Radiology, Weill Cornell Medicine, New York, New York.
[4]Dalio Institute of Cardiovascular Imaging, New York, New York.

stretching, making the foams prone to tearing at lower inflation pressures.

In this study, we have improved upon our previous work on pneumatically powered foams[13–15] by buckling the foams before actuation. When the foam is compressed in the direction opposite to our intended actuation mode, the foam attains a higher apparent elongation before break with an added benefit that the elasticity aids in actuation. While compression of porous elastomeric structures (i.e., the controlled buckling of the foam struts) has been shown to produce negative Poisson's ratio behavior,[16] shape memory properties,[17,18] directed deformation,[19,20] and actuation,[21,22] to the best of our knowledge, this article is the first to employ precompression to improve pneumatic actuation. In this study, we show that mechanical foam compression imparts buckling of the microscale struts leading to increased apparent elongation and augmented actuation (i.e., either increased displacement or reduced actuating fluid pressure).

To mold these actuators, we used an elastomeric, polyurethane (PU) open-celled foam (FlexFoam-It!; Smooth-On, Inc.) to form the inflation chamber. Because PU foams have not previously been used for fluidic actuation, to our knowledge, it is important to consider their method of foam formation as it relates to the final properties of the actuator. The foam's liquid precursors consist of three parts: (i) hydroxyl-functionalized prepolymer, (ii) water, and (iii) aromatic diisocyanate cure agent. The water serves as a chemical blowing agent that when reacting with an isocyanate at standard temperature and pressure (STP), generates carbon dioxide in an exothermic reaction, which expands to form the cells of the foam.[23] The use of elastomeric PU foams makes the fabrication of these actuators (Supplementary Fig. S1; Supplementary Data are available online at www.liebertpub.com/soro) faster than our prior method of dissolving or vaporizing embedded porogen salts.[13–15] In addition to rapid fabrication, the PU foam actuators are functional at a much higher porosity ($\phi_{pore} \sim 0.93$, prebuckled) than our previously reported polydimethylsiloxane foam actuators ($\phi_{pore} \sim 0.70$), allowing for rapid actuation ($\sim 86\%$ of maximum strain, $\varepsilon = 0.15$ in 320 ms; Supplementary Fig. S2) and lightweight devices ($\rho_{actuator} \sim 0.65$ g/cm^3).

As a potential application for these buckled foam actuators, we have also developed a patient-specific, direct cardiac compression (DCC) heart assist design. DCC devices are implanted mechanical pumps that increase blood flow in failing hearts by applying epicardial compression. Promising pneumatically actuated DCC device examples include designs with an inflatable plastic envelope within either a rigid shell[24] or a shape memory wire scaffold[25,26] surrounding the heart and a fully compliant design that uses an assembly of contracting pneumatic actuators.[27–29] The most recent of these devices demonstrates the strong need for highly complex and compliant shapes; this fluidically powered soft machine demonstrated viability through *in vivo* testing on a porcine heart.[29] Our design is similar in material properties, but it uses an elastomer foam for easy, reliable, and reproducible fabrication. Additionally, the objective of our design is primarily to address the shortcomings of other DCC devices—they largely neglect variations in patient-to-patient heart geometry and apply global compression, potentially adversely compressing coronary arteries.[30,31]

In this work, we present a DCC device design with the unique features of patient-specific fit and rapid, efficient local actuation. To form the patient-specific device, we use conventional clinical imaging techniques such as magnetic resonance imaging (MRI) or computed tomography (CT) to capture the geometry of the patient's heart (Fig. 1A). We then

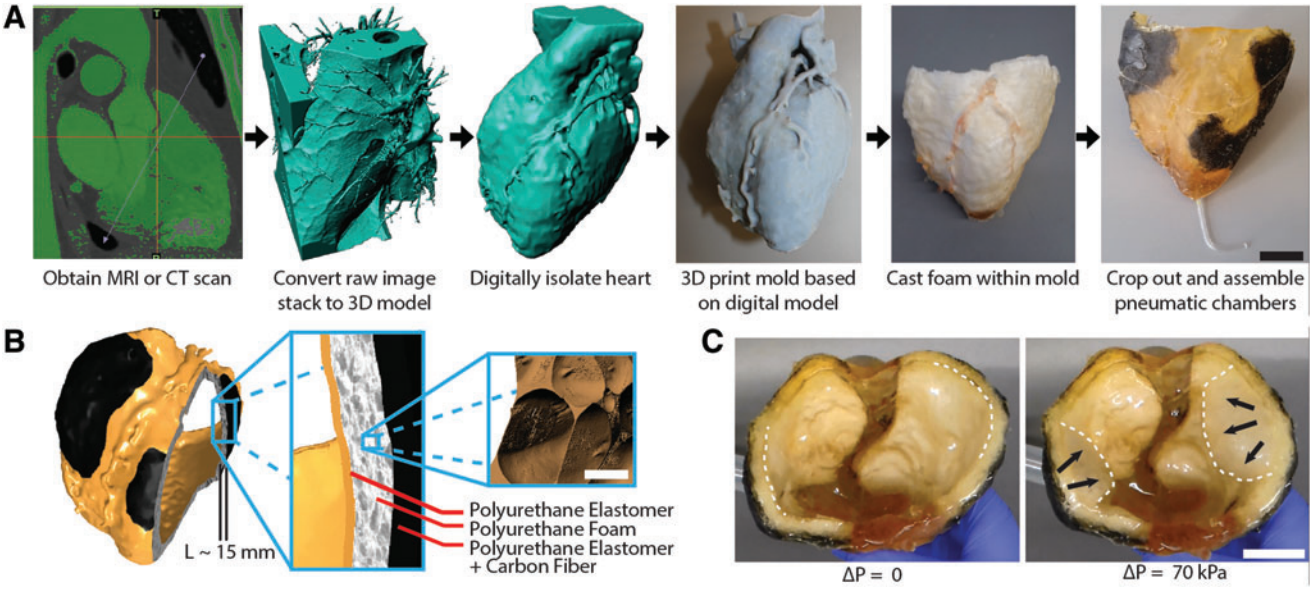

FIG. 1. The direct cardiac compression device concept. **(A)** The device fabrication process involves the following steps: collection of a chest MRI or CT of the patient's heart, reconstructing a digital 3D model of the heart, digitally isolating the heart, 3D printing a mold from the digital heart model, casting elastomer foam within the mold, and cropping and assembling two foam chambers to form the final DCC device. Scale bar, 3 cm. **(B)** A device schematic showing elastomer and strain limiting layers surrounding the foam actuation chambers. Scale bar, 250 μm. **(C)** The device before inflation (*left*) and during inflation (*right*) with *arrows* showing volume displacement upon pressurization. Scale bar, 3 cm. CT, computed tomography; DCC, direct cardiac compression; MRI, magnetic resonance imaging. Color images available online at www.liebertpub.com/soro

use the digital model of the heart as the basis of a 3D printed mold for device fabrication. The device employs pneumatically inflated, soft foam chambers (Fig. 1B, C) to apply mechanical compression on the heart muscle adjacent to the ventricles. We have demonstrated rapid DCC device fabrication (<36 h), which enables the potential for on-demand device manufacturing. Furthermore, the portion of the device that contacts the heart comprises entirely soft compliant materials that exhibit similar mechanical properties to biological tissue.[1]

By incorporating buckled foam actuators within the DCC device, it is capable of displacing large volumes of liquid ($\sim$70 mL) when inflated while remaining thin (device thickness, $L \sim 15$ mm) when deflated. Additionally, while deflating, the foam passively expels air due to its inherent elasticity. For these reasons, elastomer foams have potential operational advantages over the inflatable plastic envelopes that have been used in other designs.[24–26]

Although there are existing long-term, implantable (i.e., biocompatible) PU elastomers,[32] we chose a commercially available PU foam for this study because it rapidly fills mold cavities, cures in less than 1 h, produces a low-modulus open-celled foam with high porosity, and is of low cost. Although the materials we used in this study have not yet been tested for chronic tissue compatibility, they serve well as initial surrogate materials, in that their mechanical properties remain stable over the range of temperatures and strain rates required in the physiological environment (Supplementary Fig. S3).

Materials and Methods

Material preparation

We used all foams and elastomers as received and according to the manufacturer's instructions. We mixed the foam precursors vigorously by hand for 30 s before casting. All foam samples were FlexFoam-iT! III (Smooth-On, Inc.), except for the extending actuators which were FlexFoam-iT! V (Smooth-On, Inc.). We used a commercially available PU elastomer (VytaFlex 20; Smooth-On, Inc.) to form the nonporous impermeable coating around the foam. We selected this elastomer due to its high extensibility, $\varepsilon_{ult} = \frac{L_{failure} - L_0}{L_0} \sim 10$, and tear strength, $\Gamma = 10.5$ kN/m. We mixed the PU elastomer parts A and B in a Thinky™ planetary centrifugal mixer at 2000 rpm for 30 s before casting onto the foam. For extending actuators, we added a flexibilizing agent (So-flex, Smooth-On, Inc.) to the sealing elastomer precursor in a 1:1 weight ratio with VytaFlex part B to lower the elastomer modulus.

Actuator fabrication

We constrained the foam in compression by applying a thin coat of PU elastomer to the exterior of the cast foam before applying mechanical compression and holding until the elastomer had cured. To form the final hermetic seal, we cast a second elastomer coating (thickness, t $\sim$2 mm) around the entirety of the foam. In the case of the extending actuators shown in Figure 3, we also wrapped aramid thread (KEV138NATL01B, The Thread Exchange) circumferentially around the actuator to limit radial expansion upon inflation. Additionally, we designed all actuators to actuate parallel to the foam's rise direction. Further details of this fabrication process are in the Supplementary Data.

Tensile testing

We performed all tensile tests according to ASTM D412 on a Zwick Roell z010 instrument pulling parallel to the foam's rise direction. All tests used a 10 kN load cell at a strain rate of 5/min.

Statistical analysis

Statistics presented are *mean* $\pm$ *standard deviation* with $N = 3$ unless otherwise noted; p values were based on two-tailed Student's t-test with assumed unequal variance within the sample sets.

Microcomputed tomography imaging

We used X-ray microcomputed tomography (μCT) (ZEISS Xradia Versa 520) to image the internal structure of the foams. We used a previously described MATLAB program[13] to threshold the μCT image stacks and used ImageJ image analysis package with the BoneJ plugin[33] to determine pore characteristics. Details of the image analysis are provided in the Supplementary Data.

Blocked force testing

We performed blocked force tests by first measuring the maximum extension at a given air pressure. We then depressurized the actuator, set it on a balance with the top surface blocked with a weighted plate to ensure zero extension, and subsequently repressurized it while measuring the force exerted.

Actuator modeling

The 1D actuator model was implemented in MATLAB. We used a large deformation formulation with total stretch on the material taken as the product of the actuation stretch and precompression as relevant. We extracted foam and coating mechanical properties from their respective uniaxial tensile tests. The 1D model approximated the full 3D behavior reasonably well because the Kevlar thread provided most of the radial expansion resistance and foams have a relatively small Poisson's ratio in compression.

DCC device fabrication

Supplementary Data contain details of the conversion of an MRI or CT scan into a digital model. From the digital model of the heart, using Autodesk Maya® software and an Object30 (Stratasys) 3D printer, we designed and fabricated two sets of molds: one mold designed for casting a 20-mm-thick foam shell surrounding the heart geometry and one for compressing that foam to a thickness of 10 mm. The inset portion of the mold (i.e., the geometry of the heart) was the same for both mold sets. We first cast the PU foam into the 20-mm-thick mold. From that foam, we cut out two sections that surrounded the exterior of the ventricles and avoided the coronary artery regions. We then coated the foam sections in PU elastomer and compressed them into the 10-mm-thick mold for the duration of its cure. After demolding, we painted on an additional layer of PU elastomer (final thickness $\sim$2 mm) and manually applied a coat of 5% (by wt.) chopped carbon fiber

(Fibre Glast) in PU elastomer to the external surface so that all inflation would be directed inward.

Results

Compressed foam actuation

The void space within the foam, in addition to providing an inflatable porous network, can be exploited for mechanical advantage (Supplementary Fig. S4). To achieve this gain, we constrain the foam in a state of mechanical compression using a PU elastomer. The practical limit of uniaxial compression (i.e., complete pore collapse) is the densification strain (ε_D), which we found to be $\varepsilon_D = -0.82$ and $\varepsilon_D = -0.70$ for foams having a density of $\rho = 0.05$ and $0.08\,g/cm^3$, respectively (Fig. 2A). As we require an open porous network for inflation, we operated below ε_D for all samples.

By constraining the foam in a compressed state (Fig. 2B, C), we observed an increase in the structure's apparent ultimate strain. Specifically, for foam samples constrained uniaxially to a compression ratio ($R_c = \frac{Initial\ Volume}{Compressed\ Volume}$) of 1.5, we observed a significant ($p = 0.03$, $N = 5$) increase in apparent ultimate strain ($\varepsilon_{ult,Rc=1} = 1.20 \pm 0.12$ to $\varepsilon_{ult,Rc=1.5} = 1.59 \pm 0.26$) in uniaxial tension. This difference is nearly equal to the strain increase we would expect from the reversible unbuckling of this compression as shown in Equation (1) below:

$$\varepsilon_{expected} = \frac{L_{initial} - L_{compressed}}{L_{compressed}} = R_{c,uniaxial} - 1 = 0.5. \quad (1)$$

We attribute the discrepancy between the measured strain increase ($\varepsilon_{ult,Rc=1.5} - \varepsilon_{ult,Rc=1} \approx 0.4$) and $\varepsilon_{expected} = 0.5$ to a slight macroscopic creasing of the compressed tensile samples that initiates tearing at a lower strain (Supplementary Fig. S5). The improved elongation appears to be from a reversible structural change (i.e., strut buckling), supported by the lack of a significant difference ($p = 0.39$, $N = 5$) between the ultimate tensile stress of the samples: $\sigma_{ult,Rc=1} = 0.134 \pm 0.024$ MPa and $\sigma_{ult,Rc=1.5} = 0.148 \pm 0.024$ MPa.

Figure 2D and E shows a comparison of the porous structure of the uncompressed (i.e., $R_c = 1$) and compressed foam ($R_c = 2.5$) obtained from a μCT scan. Consistent with pore collapse, we noted a decrease in the average pore size of the compressed foam (mean pore diameter, $d_{pore} = 98 \pm 65\ \mu m$) compared with the uncompressed foam ($d_{pore} = 165 \pm 144\ \mu m$); however, the compressed pore network remained highly porous ($\phi_{Rc=2.5} = 0.85$, measured via μCT stack image analysis), enabling ample open pathways for inflation. Due to the foam's

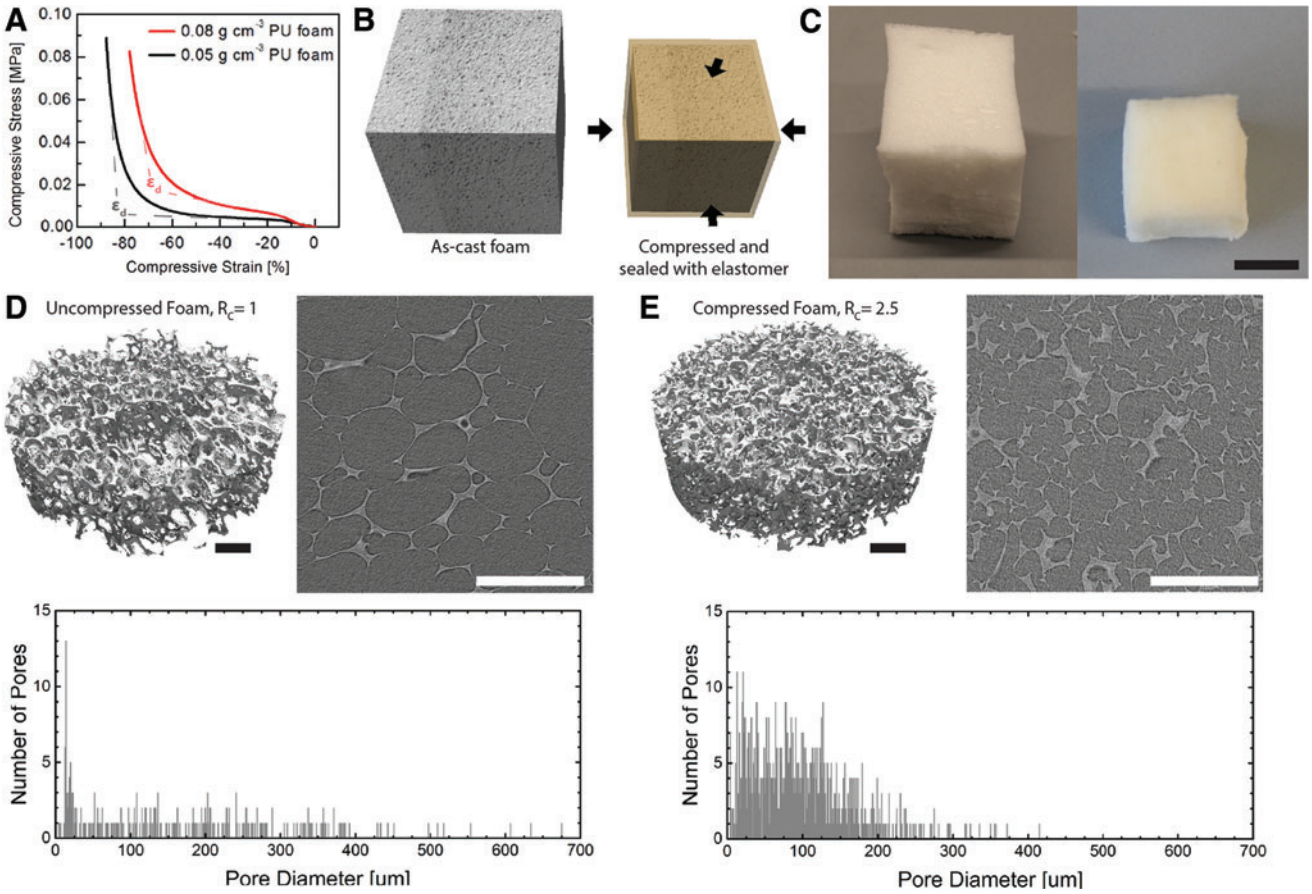

FIG. 2. The compressive behavior of polyurethane foams. **(A)** Mechanical compression of the foams used in this study, **(B)** a schematic of constrained compression method, and **(C)** a foam cube before (*left*) and after constrained triaxial compression to ~40% original volume (*right*). Scale bar, 5 mm. **(D, E)** μCT 3D reconstruction (*left*), a representative 2D slice (*right*), and pore size distribution (lower) of uncompressed and triaxially compressed foam. Scale bars, 500 μm. μCT, microcomputed tomography. Color images available online at www.liebertpub.com/soro

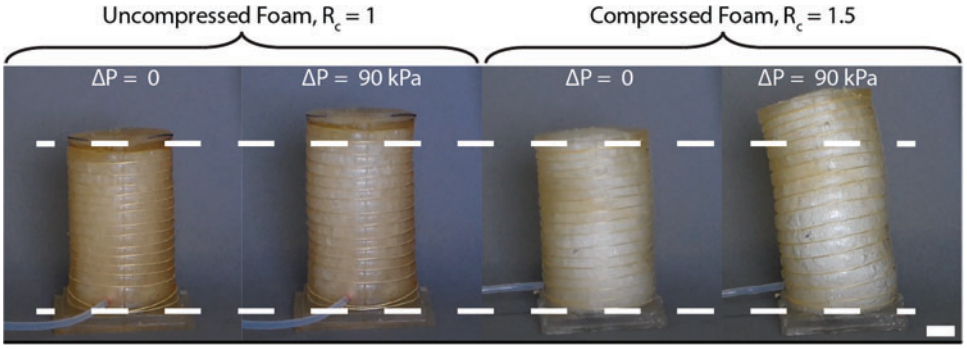

FIG. 3. The effect of foam compression on actuation. Extending actuation of an uncompressed (*left*) and compressed foam actuator (*right*). Scale bar, 5 mm. Color images available online at www.liebertpub.com/soro

high initial porosity ($\phi_{Rc=1}=0.93$), we expect an inflatable open-celled network even after large volumetric compression. For example, we estimate that a foam compressed to 20% of its initial volume (i.e., $R_c=5$) would have a porosity $\phi \sim 0.65$ (details in Supplementary Data).

The actuators can gain a mechanical advantage by starting with the foams in a compressed state. To demonstrate the more efficient actuation of actuators fabricated from compressed foams, we fabricated two extending actuators (Fig. 3); one with $R_c=1$ (no compression) and one with $R_c=1.5$ (with compression applied uniaxially). When inflated to equal pressures, the buckled foam ($R_c=1.5$) actuator showed much larger displacement than the $R_c=1$ actuator. We quantified this behavior through a blocked force test measuring both the maximum displacement (under zero load) and the maximum applied force (when constrained to zero displacement) for each actuator as a function of inflation pressure. Representative data from these measurements are shown in Table 1 with full results shown in Supplementary Fig. S6; Supplementary Table S1. These results indicate that for a given inflation pressure, the compressed foam actuator exhibited ~ 2 times the displacement and ~ 1.4 times the applied force as the one without compression. We measured this increased efficiency over uncompressed actuators in terms of displacement or force for all tested pressures in the range of 10–90 kPa.

To further understand the actuated motion, we constructed a 1D statics model to predict actuation strain as a function of inflation pressure and externally applied force. The force balance indicated that the force in the foam, the force in the coating, and the externally applied blocking force must sum to the force provided by the inflation pressure ($\sigma_{foam}\pi r^2_{actuator} + \sigma_{coating}2\pi r_{actuator}t_{coating} + F_{block} = p_{inflate}\pi r^2_{actuator}$). The stresses in the foam (σ_{foam}) and coating ($\sigma_{coating}$) were each related to their strain by the measured uniaxial stress–strain behavior. The foam strain was taken to be the actuation strain minus the precompression strain, so the required stress (and consequently required inflation pressure) was much lower to produce a given actuation strain when the precompression was large. This equation also showed the direct trade-off between blocked force and actuation strain at a given pressure. The model results for uncompressed ($R_c=1$) and compressed ($R_c=1.5$) foam actuators for the particular materials and geometry used in the experiment (Supplementary Fig. S7) show an expected 20% increase in actuation strain from the precompression. This model also indicates that the larger the radius-to-coating thickness ratio, the greater the effect.

DCC device design

As an excellent example of complex machines that could benefit from soft robotics, we applied our buckled foam system to a cardiac assist device. Specifically, we used the more efficient and thin compressed foam actuators to form a prototype DCC device. This device design applies compression to the ventricular walls, aiding the expulsion of blood. Like other pneumatically driven DCC devices,[24,26] this design avoids direct blood contact, mitigating risks associated with thrombosis and anticoagulation therapies that are present in common ventricular assist device (VAD) designs.[30,34] The use of buckled foam actuators has the potential to provide the following unique features: (i) application of localized compression on the ventricles, avoiding

TABLE 1. EXPERIMENTAL MEASUREMENTS AND MODEL PREDICTIONS FOR MAXIMUM FORCE AND ACTUATED STRAIN OF UNCOMPRESSED ($R_c=1$) AND COMPRESSED ($R_c=1.5$) ACTUATORS

	Rc = *1*		Rc = *1.5*	
Inflation pressure (kPa)	*Maximum applied force* (N)	*Maximum actuated strain*	*Maximum applied force* (N)	*Maximum actuated strain*
Experiment				
10	1.3 ± 0.4	0.017 ± 0.004	2.2 ± 0.3	0.038 ± 0.010
50	11.8 ± 1.8	0.082 ± 0.009	16.5 ± 0.2	0.182 ± 0.019
90	25.5 ± 4.4	0.155 ± 0.005	36.5 ± 4.6	0.314 ± 0.033
Model				
10	2	0.038	3.14	0.067
50	10	0.184	11.24	0.228
90	18	0.327	19.34	0.391

potentially harmful compression of coronary arteries and atria; (ii) the soft compliant materials easily deform in response to anatomical forces; (iii) the low tangent modulus ($E < 1$ MPa) and highly porous foams ($\phi > 0.93$) allow for rapid inflation and deflation at physiological rates (Supplementary Movie S1); and (iv) they can be molded to fit each patient, enabling physician-directed digital shape modification before surgery to promote reverse remodeling or inhibit ventricular aneurysms.

To demonstrate this potential, we developed a procedure to produce patient-specific 3D printed molds from standard medical imaging scans, including MRI and CT (Supplementary Fig. S8), or 3D optical scans from excised hearts (Fig. 4A), and formed a DCC device (Supplementary Fig. S9). The process began with isolating the heart as a digital model (details in Supplementary Data). From this model, we designed and fabricated 3D printed molds (Fig. 4B) to cast a foam shell around the heart geometry. From the foam shell, we excised two foam sections in regions corresponding to both ventricles while avoiding areas containing coronary arteries. These two foam chambers formed the active expanding (when inflated) portions of the DCC device; the area between the chambers (i.e., the coronary artery regions) is passive elastomer. We then constrained the foam into a smaller mold ($R_c = 2$) to buckle the foam struts (Fig. 4C). This R_c value was chosen to achieve the needed volumetric displacement based on the ultimate elongation of the foam. Although we did not optimize the R_c parameter, we could tune the parameter to increase or decrease the displacement in future versions of the device. We compressed the foam in a direction radial to the center of the heart and expect the primary expansion of the foam to be in this same direction. We then applied a strain-limiting layer of chopped carbon fiber to the exterior of the foam, which is necessary to direct the expansion of the inflated foam toward the device interior. We note that since the carbon fiber forms a transverse isotropic layer, the device applies *only* radial compression and does not twist (as the heart does during contraction). Finally, we hermetically seal the device by applying an outer coat of PU elastomer (Fig. 4D, E).

We inflated the DCC device using pressurized house air run through a regulator (model 900 dispenser, EFD-Nordson). We controlled the airflow using a three-way valve (04F30C2104AF4C05; Parker), which was activated by a microcontroller (Arduino Uno) through a relay (SRD-05VDC-SL-C; Songle). The microcontroller enabled us to dictate the frequency and duration of pulsatile inflation to mimic physiological rates. We oriented the three-way valve within the air line such that it allowed pressurized flow (for inflation) when activated and allowed venting to the atmosphere (for deflation) when deactivated. An in-line pressure sensor (PSE530-R06; SMC pneumatics) provided the inflation profile within the foam chambers.

We controlled inflation rhythms through either microcontroller code or real-time electrocardiographic (ECG) sensing (Supplementary Movie S1). While microcontroller coding allowed a stable, static, pulsatile inflation frequency and duration for benchtop tests, real-time ECG sensing is more useful within the scope of DCC as a therapeutic tool. When applying compression to the exterior of a beating heart, it is key for the device to compress in phase with the heart's rhythm.

To measure the ECG signals of the heart, we used a prepackaged heart rate monitor (AD8232; SparkFun) with electrical leads arranged in Einthoven's triangle (i.e., a constantly negative lead on the right wrist, a switching polarity lead on the

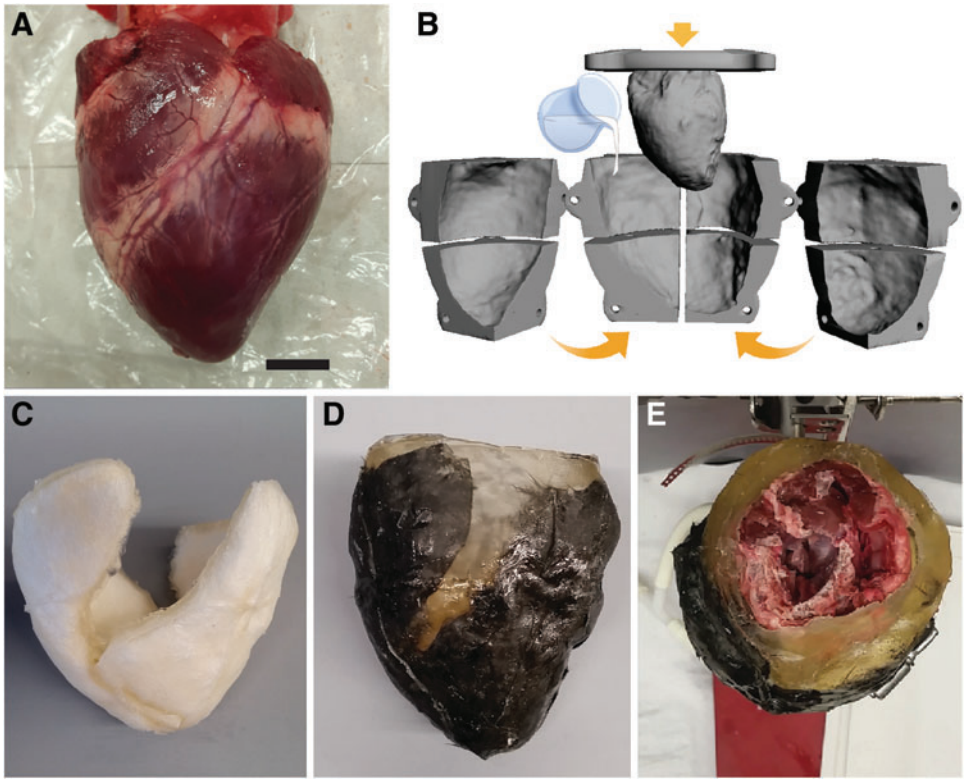

FIG. 4. Fabrication of the DCC device. **(A)** The porcine heart that served as the basis for the digitally designed mold **(B)** that was used to form an organ-specific foam shell. Scale bar, 2 cm. **(C)** The compressed foam inflation chambers that were coated in carbon fiber and sealed with elastomer to form the final DCC device **(D)** that fit well around the original heart **(E)**. Color images available online at www.liebertpub.com/soro

left wrist, and a constantly positive lead on the left ankle). This monitor collected an ECG signal that we used to control the solenoid valve, which triggered inflation of the device.

To demonstrate this DCC device, we designed one to fit a porcine heart (Supplementary Fig. S9) for an *ex vivo* test. We aimed to mimic the hemodynamics of a young pig, including a heart rate of 90 bpm, stroke volume of 70 mL, and systole and diastole durations of 220 and 440 ms, respectively.[35] Using water displacement to measure the inflated foam volume, we observed ~70 mL displacement for each chamber within a 200-ms time frame (Supplementary Fig. S10). When operating the device outside of the water, we observed (via the pressure profile) that the chambers inflated and deflated rapidly at speeds sufficient to mimic a porcine (or human) heart rate. We coordinated the inflation and deflation rhythm with a simulated electrocardiogram showing sufficiently rapid inflation to align with a native systole and diastole, respectively (Fig. 5A–C).

Finally, we performed an *ex vivo* study using the porcine heart that served as the model for the device. This experimental setup (Supplementary Fig. S11) included a pressure sensor (model ITV1031-21N2BL4, SMC) on the pneumatic line to the device and a flow sensor (SONOFLOW CO.55/120; Sonotec) on the pressurized water lines integrated into and out of the left ventricle, all of which provided real-time measurement of the air and blood surrogate (water) flow. The device's elasticity secured the heart; however, after observing the heart slightly shifting during pressurization cycles, we added a string harness to inhibit this motion.

Within the *ex vivo* study, manual massage of the heart produced ~0.18 L/min peak flow, while the DCC device produced ~0.12 L/min peak flow (Fig. 6; Supplementary Movie S1) at a frequency of 60 beats/min. Although these flows are significantly lower than the native porcine cardiac output (~5 L/min), this experiment demonstrated that the device is able to produce a repeatable, consistent flow profile and is able to impart ~67% the flow of manual massage. While the measured flow rates through the heart were lower than expected, some decrease in performance is attributed to the decreased compliance of the cadaveric heart relative to its living properties. An *in vivo* study, therefore, may show increased performance. We also note that the DCC device we fabricated was molded from a contracted heart; this choice ultimately limits the flow rate of our pump. As this article is focused on the application of buckled foam actuators and not on device efficacy, future work will focus specifically on improving the DCC device design.

Conclusions

Buckled foam actuators exhibit improved force or displacement behavior over previous foam systems; they are more efficient because they either provide a higher force or displacement at a given inflation pressure or require a lower pressure for a given force or displacement. Although we demonstrated this effect using PU foam and elastomer, the fabrication process is general and should be compatible with any variety of other open-celled elastomer materials and fluidic actuator designs.

We attribute the increased actuation behavior to the foam's elasticity. Constraining the foam in compression generated residual stresses that provided a restoring force toward the original unstressed state. Because we compressed the foam in the direction opposite to actuation, the returning force is in the direction of actuation, aiding in this motion. We note that the returning force will only be present up to the state when

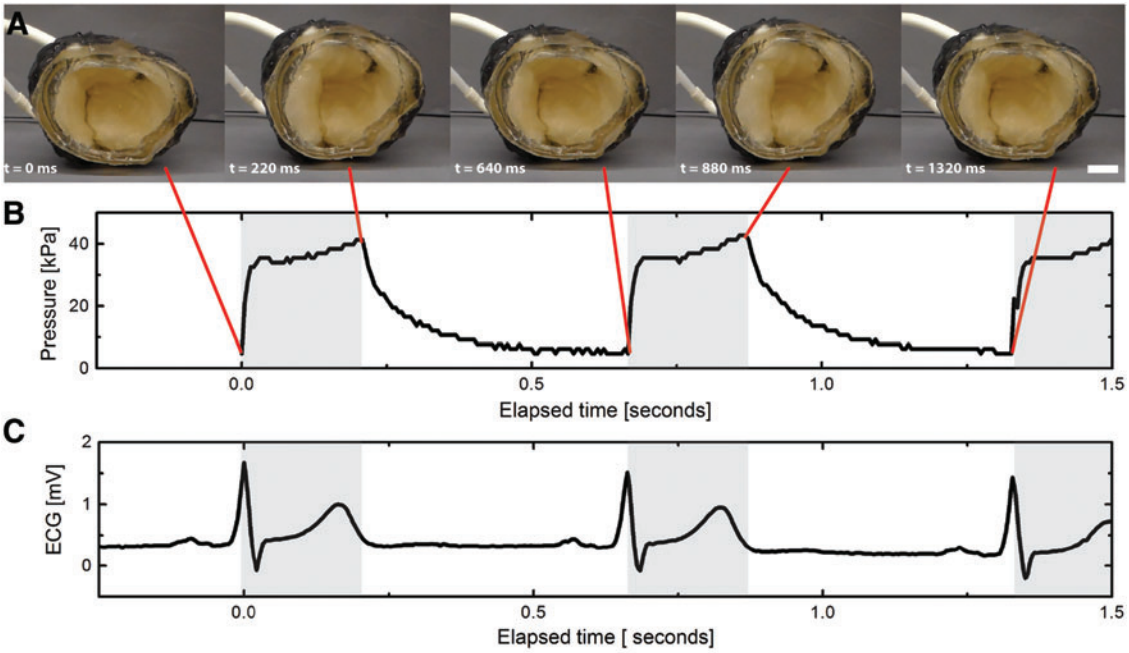

FIG. 5. DCC device benchtop and *ex vivo* performance. **(A)** Photo sequence of chamber inflation and deflation corresponding to maximum and minimum actuation pressures **(B)** recorded by an in-line analog sensor. The *shaded areas* indicate the duration of inflation triggered by a simulated ECG reading **(C)**. Scale bar, 2 cm. Video available in Supplementary Data. Color images available online at www.liebertpub.com/soro

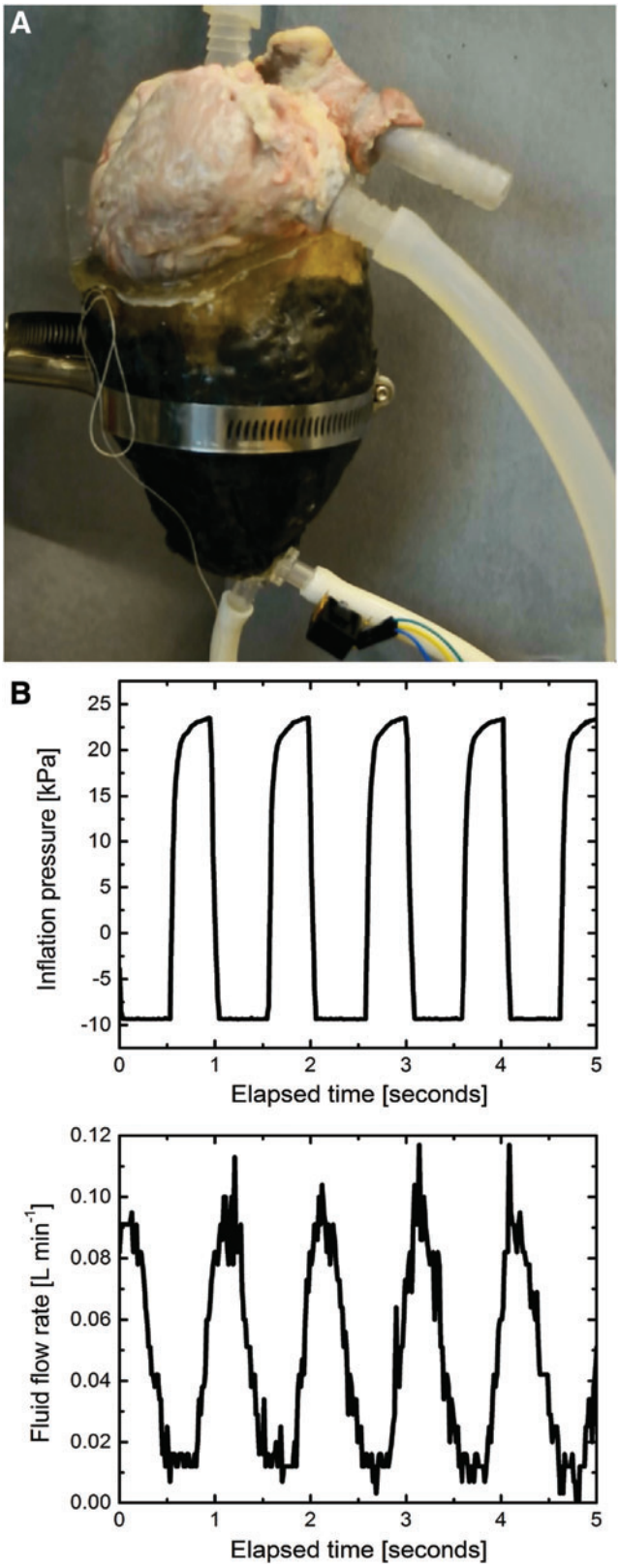

FIG. 6. *Ex vivo* demonstration on porcine heart. **(A)** The device setup for the *ex vivo* demonstration on the porcine heart with **(B)** the collected air line pressure measurements and corresponding water flow rate during *ex vivo* demonstration on the porcine heart. Video available in Supplementary Data. Color images available online at www.liebertpub.com/soro

the foam is fully unbuckled. Another benefit of buckled foam actuators is that the imparted residual stresses limit the effect of foam strain hardening. Because the compressed foam is under a lower strain when actuated, the foam tangent modulus is also lower and provides reduced resistance to expansion upon inflation.

Our demonstration DCC device formed a close fit around the porcine heart. In an *ex vivo* experiment pumping fluid through the heart, the device achieved ~67% of the peak flow rate obtained through manual massage of porcine ventricles at a duration of 500 ms for systole and 500 ms for diastole. Although we designed the device to fit a contracted heart, investigating device geometries based on different stages of the cardiac cycle would be an important direction for future studies. For example, designing the device from a heart at the end of diastole may not only minimize device effects on ventricle refilling but may also pose a risk of forming a less conformal fit around the heart.

Fabricating the device to be patient specific enables not only an optimal fit within the patient's chest cavity but is also a step toward two future possibilities. First, because this device is produced from a digital model of the patient's heart, it is possible for a physician to digitally modify the final geometry before device fabrication. This would be particularly important for patients exhibiting dilated cardiomyopathy (an enlargement of the heart, reducing its pumping efficiency). A patient-specific DCC device could be formed to the heart's healthier nonenlarged shape, potentially promoting reverse remodeling of the cardiac tissue.[36] Second, this fabrication method does not limit the device size allowing for potential adult and pediatric use alike; furthermore, for pediatric care, its compliant properties could potentially be harnessed to grow with the patient.

Additionally, the high porosity of these open-celled PU foams allowed the rapid inflation and deflation that are critical for mimicking cardiac dynamics. The repeatable ~70 mL inflation displacement within a 200-ms time frame closely mimics the heart's systole in terms of stroke volume and duration.

The fabrication time (<36 h) is currently limited by the process of 3D printing of the molds. We believe this time could be reduced to <24 h by implementing new, rapid 3D printing techniques that dramatically reduce printing times.[37]

A limitation of this DCC demonstration is that the biocompatibility of its components, to our knowledge, is not yet known. Future studies should integrate known compatible materials with accompanying fatigue tests for measuring durability over hundreds of millions of cycles (a useful lifetime for a VAD). Additionally, we intend to perform the device demonstration using fresh porcine hearts in the future in an attempt to better approximate the mechanics and dynamics of living tissue.

Acknowledgments

The authors thank Andrea Biondi and Joe Clifford for assisting in developing the MRI-digital model process, Teresa Porri for performing the μCT imaging, Roger De la Torre for aiding with the *ex vivo* test setup, and Jonathan Butcher and Anthony Ryan for their valuable discussions. This work was supported, in part, by the Air Force Office of Scientific Research under award number FA9550-15-1-0160, by a 3M

Non-Tenured Faculty Award, and a Weill Cornell Medicine CTSC TL1 traineeship (NIH/NCATS grant no. TL1TR000459). This work made use of the Cornell Center for Materials Research Shared Facilities, supported through the NSF MRSEC program (DMR-1120296). Imaging data were acquired in the Cornell BRC-Imaging Facility using the shared, NIH-funded (S10OD012287) ZEISS Xradia Versa 520 μCT.

Author Disclosure Statement

No competing financial interests exist.

References

1. Rus D, Tolley MT. Design, fabrication and control of soft robots. Nature 2015;521:467–475.
2. Dagdeviren C, Joe P, Tuzman OL, Il Park K, Lee KJ, Shi Y, *et al.* Recent progress in flexible and stretchable piezoelectric devices for mechanical energy harvesting, sensing and actuation. Extrem Mech Lett 2016;9:269–281.
3. Kaneto K. Research trends of soft actuators based on electroactive polymers and conducting polymers. J Phys Conf Ser 2016;704:12004.
4. Gu G-Y, Zhu J, Zhu L-M, Zhu X. A survey on dielectric elastomer actuators for soft robots. Bioinspir Biomim 2017; 12:11003.
5. Ionov L. Hydrogel-based actuators: possibilities and limitations. Mater Today 2014;17:494–503.
6. Polygerinos P, Correll N, Morin SA, Mosadegh B, Onal CD, Petersen K, *et al.* Soft robotics: Review of fluid-driven intrinsically soft devices; manufacturing, sensing, control, and applications in human-robot interaction. Adv Eng Mater 2017;1–22.
7. Mosadegh B, Polygerinos P, Keplinger C, Wennstedt S, Shepherd RF, Gupta U, *et al.* Pneumatic networks for soft robotics that actuate rapidly. Adv Funct Mater 2013;24: 2163–2170.
8. Galloway KC, Polygerinos P, Walsh CJ, Wood RJ. Mechanically programmable bend radius for fiber-reinforced soft actuators. 2013 16th International Conference on Advanced Robotics, ICAR Montevideo, Uruguay 2013;2013.
9. Schumacher CM, Loepfe M, Fuhrer R, Grass RN, Stark WJ. 3D printed lost-wax casted soft silicone monoblocks enable heart-inspired pumping by internal combustion. RSC Adv 2014;4:16039–16042.
10. Kwok SW, Morin SA, Mosadegh B, So JH, Shepherd RF, Martinez RV, *et al.* Magnetic assembly of soft robots with hard components. Adv Funct Mater 2014;24:2180–2187.
11. Morin SA, Kwok SW, Lessing J, Ting J, Shepherd RF, Stokes AA, *et al.* Elastomeric tiles for the fabrication of inflatable structures. Adv Funct Mater 2014;24:5541–5549.
12. Marchese AD, Onal CD, Rus D. Autonomous soft robotic fish capable of escape maneuvers using fluidic elastomer actuators. Soft Robot 2014;1:75–87.
13. Mac Murray BC, An X, Robinson SS, van Meerbeek IM, O'Brien KW, Zhao H, *et al.* Poroelastic foams for simple fabrication of complex soft robots. Adv Mater 2015;27: 6334–6340.
14. Van Meerbeek IM, Mac Murray BC, Kim JW, Robinson SS, Zou PX, Silberstein MN, *et al.* Morphing metal and elastomer bicontinuous foams for reversible stiffness, shape memory, and self-healing soft machines. Adv Mater 2016; 28:2801–2806.
15. Argiolas A, Mac Murray BC, Van Meerbeek I, Whitehead J, Sinibaldi E, Mazzolai B, *et al.* Sculpting soft machines. Soft Robot 2016;3:101–108.
16. Friis EA, Lakes RS, Park JB. Negative Poisson's ratio polymeric and metallic foams. J Mater Sci 1988;23:4406–4414.
17. Bianchi M, Scarpa F, Smith CW. Shape memory behaviour in auxetic foams: mechanical properties. Acta Mater 2010; 58:858–865.
18. Cheng NG, Gopinath A, Wang L, Iagnemma K, Hosoi AE. Thermally tunable, self-healing composites for soft robotic applications. Macromol Mater Eng 2014;299: 1279–1284.
19. Javid F, Liu J, Shim J, Weaver J, Shanian A, Bertoldi K. Mechanics of instability-induced pattern transformations in elastomeric porous cylinders. J Mech Phys Solids 2016; 96:1–17.
20. Overvelde JTB, Bertoldi K. Relating pore shape to the nonlinear response of periodic elastomeric structures. J Mech Phys Solids 2014;64:351–366.
21. Yang D, Mosadegh B, Ainla A, Lee B, Khashai F, Suo Z, *et al.* Buckling of elastomeric beams enables actuation of soft machines. Adv Mater 2015;27:6323–6327.
22. Yang D, Verma MS, So J-H, Mosadegh B, Keplinger C, Lee B, *et al.* Buckling pneumatic linear actuators inspired by muscle. Adv Mater Technol 2016;31–33.
23. Dounis D, Wilkes G. Structure-property relationships of flexible polyurethane foams. Polymer (Guildf) 1997;38: 2819–2828.
24. McConnell PI, Anstadt MP, del Rio CL, Preston TJ, Ueyama Y, Youngblood BL. Cardiac function after acute support with direct mechanical ventricular actuation in chronic heart failure. ASAIO J 2014;60:701–706.
25. Moreno MR, Harrison LD, Miller MW, Fossum TW, Nelson DA, Criscione JC. Development of a non-blood contacting cardiac assist and support device: An in vivo proof of concept study. J Med Device 2011;5:1–9.
26. Moreno MR, Harrison LD, Miller MW, Fossum TW, Nelson DA, Criscione JC. Assessment of minimally invasive device that provides simultaneous adjustable cardiac support and active synchronous assist in an acute heart failure model. J Med Device 2011;5:1–9.
27. Roche ET, Wohlfarth R, Overvelde JTB, Vasilyev NV, Pigula FA, Mooney DJ, *et al.* A bioinspired soft actuated material. Adv Mater 2014;26:1200–1206.
28. Obiajulu SC, Roche ET, Pigula FA, Walsh CJ. Soft pneumatic artificial muscles with low threshold pressures for a cardiac compression device. In Proceedings of the ASME 2013 International Design Engineering Technical Conferences and Computers and Information in Engineering Conference IDETC/CIE 2013, Portland, OR, 2013, pp. 1–8.
29. Roche ET, Horvath MA, Wamala I, Alazmani A, Song S-E, Whyte W, *et al.* Soft robotic sleeve supports heart function. Sci Transl Med 2017;9:1–12.
30. Oz MC, Artrip JH, Burkhoff D. Direct cardiac compression devices. J Heart Lung Transplant 2002;21:1049–1055.
31. Dean JW, Kuo J, Wood AJ. Myocardial infarction due to coronary artery compression by aortic root abscess. Int J Cardiol 1993;41:165–167.
32. Szycher M. Biodurable polyurethanes. In Szycher's Handbook of Polyurethanes, Second Edition, Boca Raton, FL; CRC Press: 2012, pp. 711–738.
33. Doube M, Klosowski MM, Arganda-Carreras I, Cordelières FP, Dougherty RP, Jackson JS, *et al.* Free and

extensible bone image analysis in ImageJ. Bone 2010;47: 1076–1079.
34. Silvestry SC. Histologic analysis of clots in explanted axial continuous-flow left ventricular assist devices. J Hear Lung Transplant 2015;34:616–618.
35. Hammond HK, White FC, Bhargava V, Shabetai R. Heart size and maximal cardiac output are limited by the pericardium. Am J Physiol 1992;263:H1675–H1681.
36. Starling RC, Jessup M, Oh JK, Sabbah HN, Acker MA, Mann DL, *et al.* Sustained benefits of the corcap cardiac support device on left ventricular remodeling: Three year follow-up results from the Acorn Clinical Trial. Ann Thorac Surg 2007;84:1236–1242.
37. Tumbleston JR, Shirvanyants D, Ermoshkin N, Januszewicz R, Johnson AR, Kelly D, *et al.* Continuous liquid interface production of 3D objects. Science 2015;347: 635–639.

Address correspondence to:
Robert F. Shepherd
Department of Mechanical and Aerospace Engineering
553 Upson Hall
Cornell University
Ithaca, NY 14853

E-mail: rfs247@cornell.edu